Nuclear Engineering and Technology 50 (2018) 731–737

Contents lists available at ScienceDirect

Nuclear Engineering and Technology

journal homepage: www.elsevier.com/locate/net

Original Article

Thermal transport in thorium dioxide

Jungkyu Park*, Eduardo B. Farfán, Christian Enriquez

Kennesaw State University, Department of Mechanical Engineering, Kennesaw, GA 30144, USA

ARTICLE INFO

Article history:
Received 28 September 2017
Received in revised form
20 December 2017
Accepted 12 February 2018
Available online 1 March 2018

Keywords:
Molecular Dynamics Simulation
Nuclear Fuel
Thermal Transport
Thorium Dioxide

ABSTRACT

In this research paper, the thermal transport in thorium dioxide is investigated by using nonequilibrium molecular dynamics. The thermal conductivity of bulk thorium dioxide was measured to be 20.8 W/m-K, confirming reported values, and the phonon mean free path was estimated to be between 7 and 8.5 nm at 300 K. It was observed that the thermal conductivity of thorium dioxide shows a strong dependency on temperature; the highest thermal conductivity was estimated to be 77.3 W/m-K at 100 K, and the lowest thermal conductivity was estimated to be 4.3 W/m-K at 1200 K. In addition, by simulating thorium dioxide structures with different lengths at different temperatures, it was identified that short wavelength phonons dominate thermal transport in thorium dioxide at high temperatures, resulting in decreased intrinsic phonon mean free paths and minimal effect of boundary scattering while long wavelength phonons dominate the thermal transport in thorium dioxide at low temperatures.

1. Introduction

The utilization of thorium as a new energy source has been of interest to researchers for several years [1]. Thorium exists in nature as Th-232 and is more abundant than uranium, which has been the typical nuclear fuel. Thorium is fertile and must be converted into fissile material (nuclear fuel) via a breeding process accomplished by neutron absorption in a nuclear reactor and subsequent nuclei conversions [1,2]. The resulting fissile U-233 can be used in any of several kinds of national or international nuclear reactors [1,3,4].

Thorium oxide (ThO_2), also known as thoria, has one of the highest melting points among all oxides (3573.15 K) [5]. Consequently, ThO_2 is used in light bulbs, arc-light lamps, welding electrodes, and heat-resistant materials [6–8]. As a nuclear fuel, ThO_2 has several advantages when compared to conventional uranium-based fuels. ThO_2 is relatively inert and has lower thermal expansion than UO_2. Fission gas release from ThO_2 nuclear fuel pellets is much lower than that from UO_2. In particular, its high thermal conductivity makes ThO_2 a better fuel for nuclear reactors since thermal transport is a critical issue that is directly related to the lifetime of nuclear fuels. There are several types of reactors where ThO_2 can be used as nuclear fuel: heavy water reactors, high-temperature gas-cooled reactors, boiling water reactors, pressurized water reactors, fast neutron reactors, and molten salt reactors.

The efficient thermal transport property of ThO_2 has been a subject of research for many years. In 1954, Kingery et al. [9] reported the thermal conductivity of several oxide materials including ThO_2. In 1969, Murabayashi et al. [10] reported the thermophysical properties of ThO_2 such as thermal diffusivity and thermal conductivity. More recently, Pillai and Raj [11] reported the thermal conductivity of ThO_2 using a steady-state axial heat flow comparative apparatus. There are only a few theoretical calculations for the thermal transport property of ThO_2. Ma et al. [12] reported the specific heat and thermal conductivity of ThO_2 using equilibrium molecular dynamics (MD) simulations, but the sample length is limited to 6 unit cells only.

The present study provides a meaningful addition to current literature as it presents microscopic understanding on thermal transport in ThO_2. Using classical MD along with the potential field for actinide oxides developed by Cooper et al [13–15], the thermal conductivity and the phonon mean free path of ThO_2 were obtained in this study. By progressively increasing the sample length up to 200 unit cells, the thermal conductivity of the bulk ThO_2 is estimated. Additionally, to better understand the temperature effect on thermal transport in ThO_2, thermal conductivities are estimated for ThO_2 structures at various temperatures, ranging from 100 K to 1200 K.

2. Simulation method

In this work, reverse nonequilibrium molecular dynamics (RNEMD) is employed to obtain thermal conductivity of ThO_2. The

* *Corresponding author.*
E-mail address: jpark186@kennesaw.edu (J. Park).

https://doi.org/10.1016/j.net.2018.02.002

schematic of the RNEMD simulation is shown in Fig. 1. RNEMD is a MD method for measuring transport property using cause and effect reversed algorithm first introduced by Müller-Plathe [16] and has been constantly used to estimate thermal properties of materials [17–20]. In this study, the RNEMD algorithm implemented in large-scale atomic/molecular massively parallel simulator (LAMMPS) [21] is used to create a heat flux by swapping energy between a hot bath and a cold bath in a simulation box. By the help of the periodic boundary condition, two cold baths are generated at the ends of the simulation box.

To perform RNEMD, the simulation system needs to be well-equilibrated to forget its initial thermodynamic state. Once the simulation structure is properly equilibrated, the simulation box is divided into many imaginary bins along the direction in which the thermal conductivity is to be calculated using the simulation algorithm. During the simulation, energy is swapped at each specified time step by exchanging velocity vectors of the coldest atoms in the hot region and the hottest atoms in the cold region to create a temperature gradient in the simulation structure. Energy exchange between the cold bath and hot bath occurs until the heat flow reaches a steady state. Once the heat flow in the structure reaches a steady state, the thermal conductivity, k, is calculated using the Fourier's heat conduction law with averaged heat flux and temperature gradient dT/dx as the following.

$$k = -\frac{\langle q \rangle}{\langle dT/dx \rangle}, \tag{1}$$

where $\langle q \rangle$ is the heat flux and $\langle dT/dx \rangle$ is the temperature gradient in the sample averaged over time and space. The brackets < >, indicate the average of the quantities over time as well as over the particles in the simulation cell.

The simulation structures (Fig. 1) and LAMMPS input data are constructed by using custom MATLAB programs. It must be noted that thermal transport in these structures is size dependent since phonons with wavelengths longer than the computational unit cells cannot be excited, thus limiting the overall thermal conductivity. However, the effect of simulation box boundary on thermal transport is expected to be diminished continuously as the simulation structure size increases progressively in the direction of thermal conductivity estimation (x direction in the present study) until the size of the simulation structure becomes larger than its intrinsic phonon mean free path.

In all structures simulated, the two side lengths, i.e. L_y and L_z, are constructed to be the same. In the case of ThO_2, three different side lengths ($L_y = L_z$ = 1.12 nm, 3.36 nm, and 5.6 nm) are chosen to investigate the thermal conductivity in x direction; 1.12 nm, 3.36 nm, and 5.6 nm correspond to 2, 6, and 10 unit cells, respectively. The other control parameter, i.e. the sample length, L_x, is defined as the half length of the x-direction length of the simulation structure since the characteristic length for thermal conductivity estimation in RNEMD is the distance between the hot bath located in the middle of the simulation structure and the cold bath located in the ends of the simulation structure; two identical temperature profiles are induced symmetrically after exchanging energy between the hot bath and two cold baths. Eight different sample lengths (L_x = 2.8 nm, 5.6 nm, 11.2 nm, 16.8 nm, 22.4 nm, 28 nm, 42 nm, and 56 nm) are selected for the present study; these eight different lengths are equivalent to 5, 10, 20, 30, 40, 50, 75, and 100 unit cells, respectively.

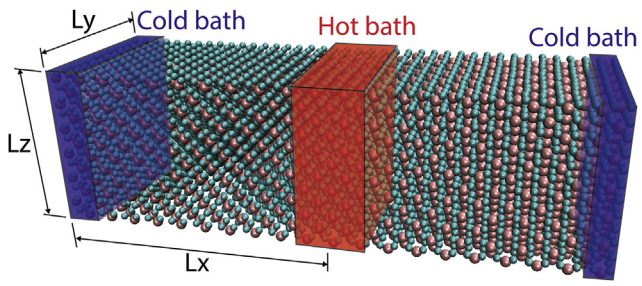

Fig. 1. Schematic of sample preparation for RNEMD.
RNEMD, reverse nonequilibrium molecular dynamics.

UO_2 structures are also constructed for comparison. For the case of thermal conductivity estimation for UO_2, the side length is fixed to be $L_y = L_z$ = 3.28 nm (6 unit cells). The sample lengths, L_x, selected for the thermal conductivity estimation of UO_2 are 5.47 nm, 10.9 nm, 16.4 nm, 21.8 nm, 27.3 nm, 41.0 nm, and 54.7 nm that are equivalent to 10, 20, 30, 40, 50, 75, and 100 unit cells, respectively.

All simulations are performed using the LAMMPS [21] code with the potential model for actinide oxides developed by Cooper and Rushton [13–15], which takes into account many body effects to improve the description of thermophysical properties of actinide oxides. The potential model uses the embedded atom method to allow the inclusion of many body interaction during MD simulations, and its functional consists of pairwise and many body components as follows.

$$E_i = \frac{1}{2}\sum_j \phi_{\alpha\beta}(r_{ij}) - G_\alpha \sqrt{\sum_j \sigma_\beta(r_{ij})}, \tag{2}$$

where E_i is the energy of ith atom with respect to all other atoms, r_{ij} is the distance between ith atom and jth atom, and α and β denote the species of ith atom and jth atom, respectively. The first term in the Eq. (2) represents pairwise interaction between ith atom and jth atom, separated by r_{ij} and it includes long range electrostatic contributions and short range contributions. The short range contributions to the potential energy are based on the potential model developed by Morse [22] and Buckingham [23]. The second term in the Eq. (2) introduces many body perturbation to the pairwise interaction by summing a set of pairwise functions, $\sigma_\beta(r_{ij})$, between ith atom and its surrounding atoms. As can be seen in the Eq. (2), many body perturbation is proportional to the square root of the summation of pairwise functions, where G_σ is the proportionality constant. The detailed information for the functional can be found in Cooper et al. [13]. This potential model has successfully predicted thermophysical properties of actinide solids such as thermal expansion and specific heat capacity [13]. More recently, it has been employed to calculate the diffusion properties of CeO_2, ThO_2, and UO_2 [14,24] as well as the thermal conductivity of UO_2 [25].

The simulation structure is energy-minimized first by iteratively adjusting atomic coordinates to get a near 0 K structure. Once energy-minimization is finished, the temperature is elevated to 500 K using isenthalpic (NPH) ensemble with Langevin thermostat for faster equilibration. Then, the system is cooled down to room temperature with isothermal–isobaric (NPT) ensemble and equilibrated. RNEMD is carried out on the equilibrated structures for 2 ns with micro-canonical (NVE) ensemble with a time-step of 1 fs.

3. Results and discussion

The temperature profile obtained after imposing a heat flux for 2 ns is shown in Fig. 2. The temperature slips at the boundaries result from the unphysical manner by which heat is added/removed at the hot and cold baths [20,26–28]—the continuous discharge of low/high temperature atoms in the hot/cold bath is not compensated timely by the diffusion of low/high temperature atoms from

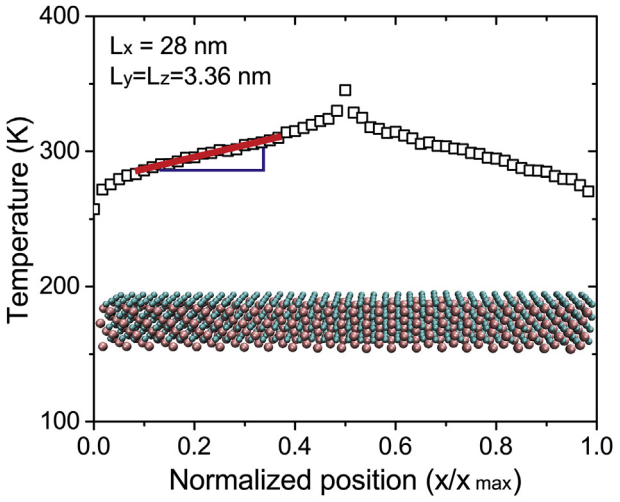

Fig. 2. A representative temperature profile during RNEMD. The thermal gradient is obtained from the linear portion of the temperature profile using the linear regression function in MATLAB.
RNEMD, reverse nonequilibrium molecular dynamics.

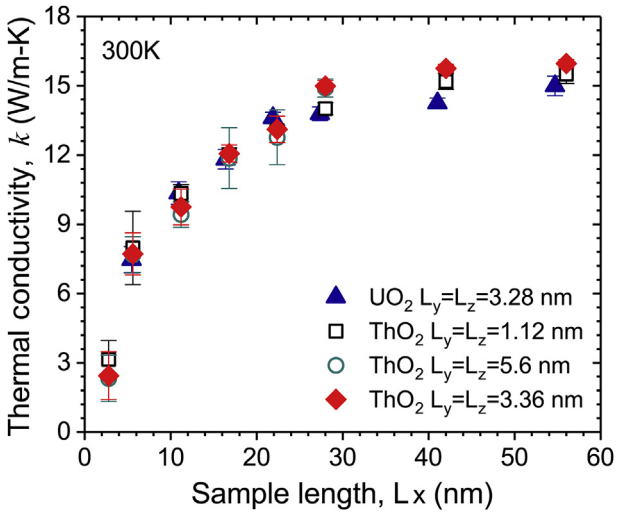

Fig. 3. The thermal conductivity estimation of ThO_2 structures using RNEMD. L_y and L_z denote side lengths and L_x is the sample length which is the half size of the total simulation box length.
RNEMD, reverse nonequilibrium molecular dynamics.

neighboring bins because of the fast energy swapping rate [29]. However, extracting thermal conductivity from this nonlinear temperature profile can be easily achieved by discarding the regions close to the hot and cold baths and taking only the linear portion of the profile.

Table 1 lists the dimensions of all the simulation structures employed in the present work along with the room temperature thermal conductivities obtained by using the method described in the simulation method section. The results presented in Table 1 are plotted in Fig. 3 for clarity. The thermal conductivity measurements for the structures with the sample lengths (L_x) of 42 nm and 56 nm and the side lengths (L_y or L_z) of 5.6 nm are prohibited computationally because of the large number of atoms; the biggest structure simulated in this study contains 120,000 atoms when $L_x = 28$ nm and $L_y = L_z = 5.6$ nm.

ThO_2 exhibits higher thermal conductivities than UO_2 especially when structure size becomes large. This superior thermal conductivity of ThO_2 has been reported repeatedly, and researchers suggested mixing UO_2 together with ThO_2 to improve its thermal transport property [10,30–32]. A strong dependency of the thermal conductivity on the sample length is observed in all cases. The thermal conductivity increases with an increase in the sample length. This dependency indicates the room temperature phonon mean free path of ThO_2 is larger than or comparable to the structure sizes simulated in this study. Therefore, in addition to phonon–phonon scattering, scattering at the boundaries of the simulation box influences the thermal conductivity of the sample simulated here. An interesting behavior is seen when the trend of thermal conductivity increase in UO_2 is compared to that in ThO_2 (Fig. 3); the thermal conductivity of UO_2 reaches the plateau phase faster than that of ThO_2 as sample length is increased. This indicates that the intrinsic phonon mean free of UO_2 is shorter than ThO_2.

It should also be noted that the side length affects the thermal conductivities of ThO_2 even when the sample lengths are the same. The effect of the side length does not show a consistent tendency until the sample length becomes 28 nm. From the sample length of 28 nm, it is observed that a structure with larger side length shows a slightly bigger thermal conductivity than a structure with smaller side length, provided that the sample lengths of the both structures are the same. This side length effect is expected to exist until the side length is increased above the intrinsic phonon mean free path of ThO_2. However, the effect of side length on the thermal conductivity is minimal (comparable to the measurement errors during RNEMD) when compared to the effect of the sample length as shown in Fig. 3. This indicates that thermal transport in x direction is not altered much by the boundary scatterings from x-y or x-z planes, and the effect of cross-sectional area can be ignored during the thermal conductivity estimation using RNEMD. This is consistent with other thermal transport studies that utilized MD [33–35], where researchers identified a minimal effect of cross-sectional area on thermal conductivity calculation.

On the basis of the kinetic theory of phonon transport, the thermal conductivity is proportional to the phonon mean free path. In the case where phonons scatter at the heat reservoir, the effective mean free path, l_{eff}, can be expressed using Matthiessen rule [36,37] as.

$$\frac{1}{l_{eff}} = \frac{1}{l_{ph-ph}} + \frac{1}{l_b} \tag{3}$$

Table 1
Thermal conductivities of ThO_2 and UO_2 at room temperature obtained from RNEMD.

Structure			Thermal conductivity, k (W/m-K)						
ThO_2	Sample length, L_x		5.6 nm	11.2 nm	16.8 nm	22.4 nm	28.0 nm	42.0 nm	56.0 nm
	Side length, $L_y = L_z$	1.12 nm	7.9 ± 1.5	10.3 ± 0.3	11.9 ± 0.3	13.0 ± 0.2	14.0 ± 0.2	15.1 ± 0.3	15.5 ± 0.4
		3.36 nm	7.7 ± 0.9	9.7 ± 0.7	12.0 ± 0.3	13.1 ± 0.5	14.5 ± 0.2	15.7 ± 0.1	15.9 ± 0.1
		5.60 nm	7.6 ± 0.7	9.4 ± 0.5	11.8 ± 1.3	12.7 ± 1.1	14.8 ± 0.3	—	—
UO_2	Sample length, L_x		5.47 nm	10.9 nm	16.4 nm	21.8 nm	27.3 nm	41.0 nm	54.7 nm
	Side length, $L_y = L_z$	3.28 nm	7.4 ± 0.5	10.3 ± 0.4	11.8 ± 0.4	13.6 ± 0.2	13.7 ± 0.2	14.2 ± 0.2	14.9 ± 0.4

RNEMD, reverse nonequilibrium molecular dynamics.

where $l_{ph\text{-}ph}$ is phonon–phonon scattering length, and l_b is the phonon–boundary scattering length due to simulation box boundary. As discussed earlier, the dominant scale factor that limits thermal transport in ThO_2 is sample length (L_x), and side lengths (L_y and L_z) show negligible effect. Therefore, the phonon–boundary scattering length, l_b, can be approximated to be sample length. Then, using Eq. (3) along with the kinetic theory of phonon transport, the thermal conductivity of the sample can be expressed as.

$$\frac{1}{k} \propto \frac{1}{l_{eff}} = \frac{1}{l_{ph-ph}} + \frac{1}{l_b}. \tag{4}$$

This relationship implies that the inverse of the thermal conductivity, k, versus inverse of the system size, l_b, is a linear curve and that the thermal conductivity for an infinitely large structure can be obtained by simple extrapolation of the plot, i.e., in the limit when $1/l_b \rightarrow 0$.

For the estimation of bulk thermal conductivity, the simulation structures with the side length of 3.36 nm are selected and the inverse of the thermal conductivity is plotted as a function of the inverse of the size of the sample length in Fig. 4. The linear relation between the two parameters, i.e. 1/thermal conductivity and 1/length, shown in Fig. 4 confirms the effectiveness of Matthiessen's rule once again. In accordance with Eq. (4), extrapolating the linearly fitted line to the y-axis with $x = 0$ provides an estimate of thermal conductivity for an infinitely large ThO_2, i.e. 20.8 W/m-K. The thermal conductivity of bulk UO_2 is estimated to be 17.1 W/m-K by using the same method.

Although there are several thermal conductivity measurement results available in the literature for ThO_2, more data are still needed to fully understand the thermal transport in ThO_2. Several researchers [38–40] reported a range of 10–15 W/m-K as the thermal conductivity of ThO_2 at 300 K by utilizing thermal diffusivity measurements. More recently, Pillai and Raj [11] reported 11 W/m-K as the thermal conductivity of ThO_2 at 300 K using a steady-state axial heat flow comparative apparatus. Researchers also calculated the thermal conductivity of ThO_2 using MD, and they reported thermal conductivity values that are slightly higher than the experimental results in the past. For example, Ma et al. [12] reported ca. 16.5 W/m-K as the thermal conductivity of a ThO_2 structure with ~3.3 nm at 300 K. Behera and Deo [41] reported ca. 22 W/m-K for a ThO_2 structure with ~3.3 nm length. Cooper et al. [35] reported ca. 12 W/m-K as the thermal conductivity of a ThO_2 structure with 16 nm. Rahman et al. [42] also used nonequilibrium MD with the same force field that is used in the present work to report 15.9 W/m-K as the thermal conductivity of ThO_2 with the simulation box size of 200 unit cells. Our estimate of 15.9 W/m-K for ThO_2 with 200 unit cells is consistent with the results mentioned above. However, it must be noted that the above calculations using MD do not reflect the effect of porosity and needs to be adjusted by considering the reduced density of ThO_2 to match with the experimental measurements; any defect or porosity in ThO_2 is expected to significantly alter the lattice vibration in ThO_2, resulting in reduced thermal conductivity. In this regards, Bakker et al. [31] suggested that the thermal conductivity of ThO_2 should be corrected by using a relationship, $f = (1 - P)^{1.5}$, where P ($0 < P < 1$) is the porosity and f ($0 < f < 1$) is the fraction of the thermal conductivity. Recently, Szpunar et al. [43] adjusted their theoretical thermal conductivity calculations of ThO_2 to account for 5% porosity by using the same relationship. When the same correlation is applied, the thermal conductivity of ThO_2 with 200 unit cells in this research (15.9 W/m-K) is adjusted to be 14.7 W/m-K while the thermal conductivity estimate of bulk ThO_2 (20.8 W/m-K) is adjusted to become 19.2 W/m-K if 5% porosity is considered. In addition, it should be mentioned that the results of classical MD highly depend on the quality of the force field used. Therefore, the MD results need to be compared with other theoretical calculations that utilize the first principles approach. Xiao et al. [44] reported ~ 13 W/m-K as the thermal conductivity of ThO_2 by using the Slack expression [45]. Lu et al. [46] estimated the thermal conductivity of ThO_2 to be ~12 W/m-K by using density functional theory calculations. Malakkal et al. [47] used two different pseudopotentials to calculate the lattice thermal conductivity of ThO_2 and reported ~18 W/m-K at 400 K. Szpunar et al. [43,48] reported ~16 W/m-K for the thermal conductivity of ThO_2 at 300 K. The latest theoretical calculations for the thermal conductivity of ThO_2 were performed by Szpunar et al. [49] who reported a thermal conductivity value of 18 W/m-K for ThO_2 at 400 K.

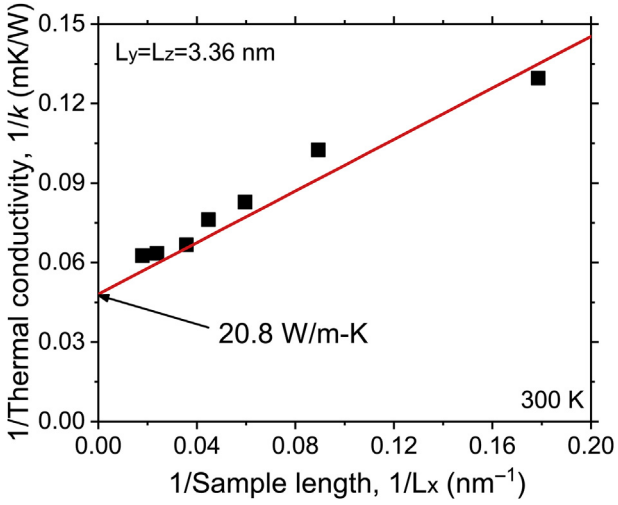

Fig. 4. The reciprocal of thermal conductivity is plotted as a function of the inverse of sample length to estimate the thermal conductivity of an infinitely large ThO_2 structure.

The bulk thermal conductivity value obtained above can be used to estimate the intrinsic phonon mean free path by using the kinetic theory of gas [50,51]. Thermal conductivity can be related to phonon mean free path as

$$k = \frac{1}{3} c v_g l_p, \tag{5}$$

where, c is specific heat per volume, v_g is average group velocity, and l_p is phonon mean free path. Eq. (5) can transformed to give the expression for phonon mean free path as

$$l_p = \frac{3k}{c v_g}. \tag{6}$$

Several researchers [31,46,52–56] reported the specific heat values for ThO_2 ranging from 0.2234 to 0.2689 J/g-K at room temperature. The value $v_g = 3317.3$ m/s reported by Lu et al. [57] is used as the value for the average phonon group velocity for the phonon mean free path calculation. If the bulk thermal conductivity value obtained in this study (20.8 W/m-K) is used, the phonon mean free path is expected to be between 7 nm and 8.5 nm. As observed in Fig. 3, the thermal conductivity begins to reach the plateau when the sample lengths become longer than 10 nm. This can be attributed to the phonon mean free path shorter than 10 nm; as the sample length becomes longer than the phonon mean free path, phonon scattering from the simulation box boundaries becomes greatly reduced, resulting in the termination of the ballistic thermal transport stage.

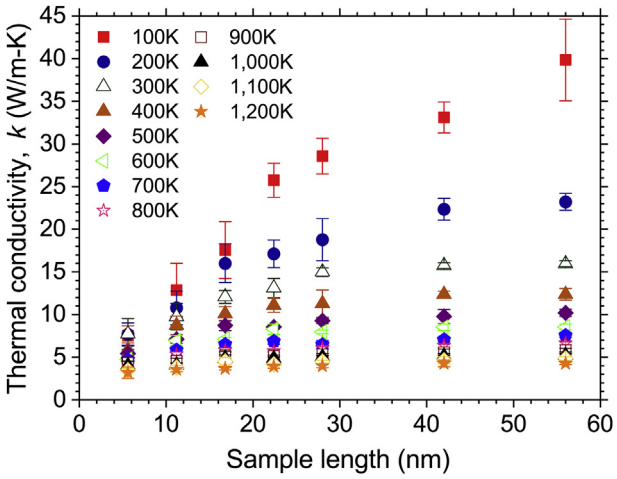

Fig. 5. Thermal conductivities of ThO_2 structures with various sample lengths at different temperatures.

To better understand phonon transport in ThO_2, the thermal conductivities of ThO_2 structures with seven different lengths (5.6 nm, 11.2 nm, 16.8 nm, 22.4 nm, 28.0 nm, 42.0 nm, and 56.0 nm) were estimated at various temperatures, ranging from 100 K to 1200 K using RNEMD. The total 84 (7 sample lengths × 12 temperature points) thermal conductivity estimation results are plotted in Fig. 5. From this figure, it is clearly identified that the increase in the temperature degrades the thermal transport property of ThO_2; the simulation structure with higher temperature always exhibits lower thermal conductivity. This phenomenon is attributed to Umklapp phonon–phonon scattering at high temperatures. At high temperatures the population of phonons with large momenta is increased. These phonons with large momenta often lose their energy when they are collided with other phonons with high momenta since the total resulting momenta easily exceeds the allowed momentum in the lattice structure. Therefore, the increased Umklapp scattering at high temperatures results in the decrease of the thermal transport efficiency. Moreover, it is observed that at high temperatures the thermal transport in ThO_2 is not limited by the sample length; the thermal conductivity does not show significant increase with an increase in the sample length at 1200 K while the thermal conductivity rapidly increases with an increase in the sample length at 100 K. This can be well explained by the dominant phonon wavelength in a system that depends on temperature. Dominant wavelength, λ_d, for thermally excited phonon can be estimated using $\hbar\omega_d = h\nu/\lambda_d \approx k_B T$ [58], where h is the Planck constant, $\hbar = h/2\pi$, k_B is the Boltzmann constant, ν is the phonon group velocity, ω_d is the dominant phonon frequency, and T is the temperature. Average phonon group velocity is estimated from $\overline{\nu}(T) = \frac{\sum_{k,s} \nu(k,s)\overline{n}(k,s)}{\sum_{k,s} \overline{n}(k,s)}$ [59], where k is wavenumber, s is phonon branch, $\nu(k,s)$ is phonon group velocity, and $\overline{n}(k,s)$ is Bose-Einstein distribution. As can be seen in this relation, the wavelength of dominant phonon modes decreases with an increase in the temperature of the system. Therefore, at low temperatures, long wavelength phonons are expected to dominate the thermal transport in the system, and they are not likely to participate in Umklapp scattering because of their short wavenumbers. Recently, Kim et al. [60] decomposed the contribution of acoustic phonons and optical phonons to the thermal conductivity of UO_2 to show that the lattice

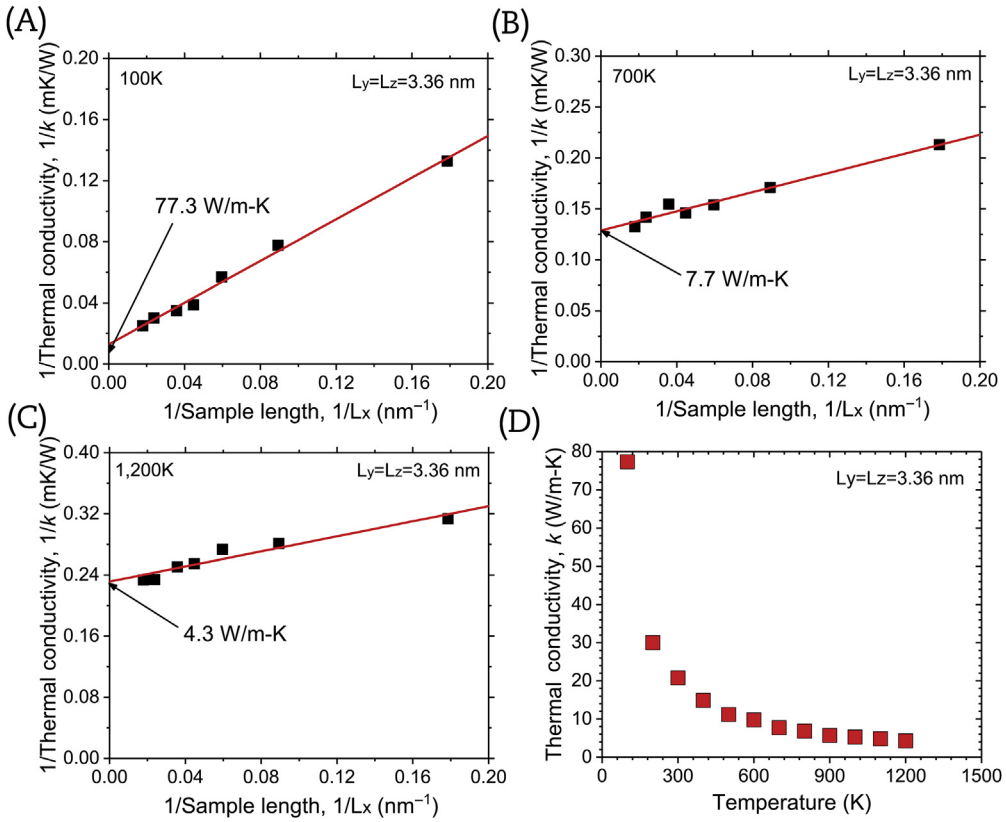

Fig. 6. The bulk thermal conductivity evaluation of ThO_2 using Matthiessen's rule. (A) At 100 K. (B) At 700 K. (C) At 1200 K. (D) The bulk thermal conductivity of ThO_2 at different temperatures.

thermal conductivity of UO_2 is dominated by the long-range acoustic phonons. However, it is worth noting that the importance of optical phonons in the thermal transport of actinide oxides has been raised by researchers including Pang et al. [61] who showed that in the case of UO_2, longitudinal optical phonon modes carry the largest amount of heat, in contrast to past simulation results. It is true that the longitudinal optical phonons have relatively high group velocities and a possibility to carry a large amount of heat, but further investigations are required since there are two contradicting opinions among researchers. At high temperatures, on the other hand, the majority phonons are the ones with short wavelength that are usually engaged in Umklapp scattering, and this shortens the intrinsic phonon mean free path in the sample; phonons experience substantial Umklapp scattering before they are scattered by the boundaries, resulting in minimal effect of boundary scattering.

In addition, the bulk thermal conductivities of ThO_2 were evaluated at different temperatures by employing Matthiessen's rule (Fig. 6). From Fig. 6D, it is observed that the thermal conductivity of ThO_2 decreases with increasing temperature; the highest thermal conductivity is estimated to be 77.3 W/m-K at 100 K while the lowest thermal conductivity is estimated to be 4.3 W/m-K at 1200 K. This temperature effect can also be identified in the Figs. 6A–6C, where the reciprocal of thermal conductivity is plotted as a function of the reciprocal of sample length. The clear linear relationship between $1/k$ and $1/L_x$ in Fig. 6A indicates that the major phonon scattering mechanism in the simulated structure is boundary scattering which is directly related to the sample length. At high temperatures (Fig. 6C), however, the clear linear relationship between $1/k$ and $1/L_x$ is less evident since the majority of phonons are scattered by Umklapp scattering rather than boundary scattering. With this regards, Pillai and Raj [11] also identified that the intrinsic phonon thermal conductivity of ThO_2 decreases with an increase in temperature. Murabayashi et al. [10] used the flash method that employs laser pulses to measure the thermal conductivity of ThO_2 and also identified that thermal conductivity of ThO_2 decreases with increasing measurement temperature. More recently, Szpunar et al. [43,48] successfully related the inverse of the thermal conductivities of ThO_2 with the inverse of temperature using the relationship $1/k = 1/(A + BT)$ where k is thermal conductivity, A and B are constants, and T is temperature, to account for increased phonon–phonon scattering due to the increased temperature.

4. Conclusions

A RNEMD along with the potential field for actinide oxides developed by Cooper and Rushton [13–15] is employed to study thermal transport in ThO_2. The results confirmed again that ThO_2 has a higher thermal conductivity than UO_2. The simulations also reveal the existence of ballistic thermal transport in ThO_2 when the structure size is smaller than its phonon mean free path (7–8.5 nm); the thermal conductivity of ThO_2 almost linearly increases with an increase in the sample length until the sample length becomes bigger than 10 nm. However, the thermal conductivity of ThO_2 is not altered by the change in the sectional area of sample, indicating the minimal effect of a sectional area on the phonon transport in ThO_2. By utilizing the thermal conductivities of ThO_2 structures with different sample lengths together with Matthiessen's rule, the room temperature thermal conductivity of bulk ThO_2 was computed to be 20.8 W/m-K that is higher than previously reported values. In addition, by performing RNEMD simulations at different temperatures, it was concluded that thermal transport in ThO_2 at high temperatures is governed by Umklapp phonon–phonon scattering. Moreover, it was observed that at high temperatures thermal transport in ThO_2 is not impeded by the sample length unlike the room temperature thermal transport because of the short wavelength of the dominant phonon modes; phonons with short wavelength are scattered by the Umklapp phonon–phonon scattering mechanism well before they reach the simulation box boundaries. The thermal conductivity of bulk ThO_2 was inversely proportional to the measurement temperature. The highest bulk thermal conductivity was measured to be 77.3 W/m-K at 100 K while the lowest bulk thermal conductivity was computed to be 4.3 W/m-K at 1200 K.

Conflicts of interest

The authors declare that there is no conflict of interests regarding the publication of this paper.

Acknowledgments

This work made use of the High Performance Computing Resource at Kennesaw State University. This research did not receive any specific grant from funding agencies in the public, commercial, or not-for-profit sectors.

References

[1] J. Belle, R. Berman, Thorium Dioxide: Properties and Nuclear Applications, USDOE Assistant Secretary for Nuclear Energy, Office of Naval Reactors, Washington, DC, 1984.
[2] M.S. Kazimi, Thorium fuel for nuclear energy, Am. Sci. 91 (5) (2003) 408–415.
[3] M. Lung, O. Gremm, Perspectives of the thorium fuel cycle, Nucl. Eng. Des. 180 (2) (1998) 133–146.
[4] M. Todosow, A. Galperin, S. Herring, M. Kazimi, T. Downar, A. Morozov, Use of thorium in light water reactors, Nucl. Technol. 151 (2) (2005) 168–176.
[5] W.A. Lambertson, M.H. Mueller, F.H. Gunzel, Uranium oxide phase equilibrium systems: IV, UO2–ThO2, J. Am. Ceram. Soc. 36 (12) (1953) 397–399.
[6] P. Lidster, H. Bell, The Application of Thoria Yttria Electrolytes in Measuring the Thermodynamic Properties of Chromium in Alloys, Univ. of Newcastle-upon-Tyne, Eng, 1969.
[7] E.F. Schubert, J.K. Kim, Solid-state light sources getting smart, Science 308 (5726) (2005) 1274–1278.
[8] A. Breslin, W. Harris, Use of Thoriated Tungsten Electrodes in Inert Gas Shielded Arc Welding—Investigation of Potential Hazard, Am. Ind. Hyg. Assoc. Q 13 (4) (1952) 191–195.
[9] W.D. Kingery, J. Francl, R. Coble, T. Vasilos, Thermal conductivity: X, data for several pure oxide materials corrected to zero porosity, J. Am. Ceram. Soc. 37 (2) (1954) 107–110.
[10] M. Murabayashi, S. Namba, Y. Takahashi, T. Mukaibo, Thermal Conductivity of ThO2-UO2 System, J. Nucl. Sci. Technol. 6 (3) (1969) 128–131.
[11] C. Pillai, P. Raj, Thermal conductivity of ThO 2 and Th 0.98 U 0.02 O 2, J. Nucl. Mater. 277 (1) (2000) 116–119.
[12] J.-J. Ma, J.-G. Du, M.-J. Wan, G. Jiang, Molecular dynamics study on thermal properties of ThO 2 doped with U and Pu in high temperature range, J. Alloy. Comp. 627 (2015) 476–482.
[13] M. Cooper, M. Rushton, R. Grimes, A many-body potential approach to modelling the thermomechanical properties of actinide oxides, J. Phys. Condens. Matter 26 (10) (2014) 105401.
[14] M.W. Cooper, S.T. Murphy, P.C. Fossati, M.J. Rushton, R.W. Grimes, Thermophysical and anion diffusion properties of (Ux, Th1−x) O2, Proc. R. Soc. Lond. A Math. Phys. Eng. Sci. 470 (2171) (2014) 20140427. The Royal Society.
[15] M. Cooper, S. Murphy, M. Rushton, R. Grimes, Thermophysical properties and oxygen transport in the (U x, Pu 1−x) O 2 lattice, J. Nucl. Mater. 461 (2015) 206–214.
[16] F. Muller-Plathe, A simple nonequilibrium molecular dynamics method for calculating the thermal conductivity, J. Chem. Phys. 106 (14) (1997) 6082–6085.
[17] J. Park, M.F. Bifano, V. Prakash, Sensitivity of thermal conductivity of carbon nanotubes to defect concentrations and heat-treatment, J. Appl. Phys. 113 (3) (2013), 034312–034312-11.
[18] J. Park and V. Prakash, "Thermal Resistance Across Interfaces Comprising Dimensionally Mismatched Carbon Nanotube-graphene Junctions in 3D Carbon Nanomaterials."
[19] J. Park, V. Prakash, Thermal transport in 3D pillared SWCNT–graphene nanostructures, J. Mater. Res. 28 (2013) 940–951.
[20] J. Park, V. Prakash, Phonon scattering and thermal conductivity of pillared graphene structures with carbon nanotube-graphene intramolecular junctions, J. Appl. Phys. 116 (2014).
[21] S. Plimpton, P. Crozier, A. Thompson, LAMMPS-large-scale atomic/molecular massively parallel simulator, Sandia National Laboratories, 2007.

[22] P.M. Morse, Diatomic molecules according to the wave mechanics. II. Vibrational levels, Phys. Rev. 34 (1) (1929) 57.
[23] R.A. Buckingham, The classical equation of state of gaseous helium, neon and argon, Proc. R. Soc. Lond. A Math. Phys. Eng. Sci. 168 (933) (1938) 264–283. The Royal Society.
[24] M. Cooper, R. Grimes, M. Fitzpatrick, A. Chroneos, Modeling oxygen self-diffusion in UO 2 under pressure, Solid State Ionics 282 (2015) 26–30.
[25] M. Qin, et al., Thermal conductivity and energetic recoils in UO2 using a many-body potential model, J. Phys. Condens. Matter 26 (49) (2014) 495401.
[26] Y.-G. Yoon, R. Car, D.J. Srolovitz, S. Scandolo, Thermal conductivity of crystalline quartz from classical simulations, Phys. Rev. B 70 (1) (2004) 012302.
[27] S. Stackhouse, L. Stixrude, Theoretical methods for calculating the lattice thermal conductivity of minerals, Rev. Mineral. Geochem. 71 (1) (2010) 253–269.
[28] F. Müller-Plathe, D. Reith, Cause and effect reversed in non-equilibrium molecular dynamics: an easy route to transport coefficients, Comput. Theor. Polym. Sci. 9 (3) (1999) 203–209.
[29] S. Kuang, Atomistic Simulations of Nanoscale Transport Phenomena, 2012.
[30] S. Motoyama, Y. Ichikawa, Y. Hiwatari, A. Oe, Thermal conductivity of uranium dioxide by nonequilibrium molecular dynamics simulation, Phys. Rev. B 60 (1) (1999) 292.
[31] K. Bakker, E. Cordfunke, R. Konings, R. Schram, Critical evaluation of the thermal properties of Th02 and Th1− yUy02 and a survey of the literature data on Th1− yPuy02, J. Nucl. Mater. 250 (1) (1997) 1–12.
[32] T. Kutty, et al., Development of CAP process for fabrication of ThO 2–UO 2 fuels Part II: Characterization and property evaluation, J. Nucl. Mater. 373 (1) (2008) 309–318.
[33] P.K. Schelling, S.R. Phillpot, P. Keblinski, Comparison of atomic-level simulation methods for computing thermal conductivity, Phys. Rev. B 65 (14) (2002) 144306.
[34] T. Watanabe, S.B. Sinnott, J.S. Tulenko, R.W. Grimes, P.K. Schelling, S.R. Phillpot, Thermal transport properties of uranium dioxide by molecular dynamics simulations, J. Nucl. Mater. 375 (3) (2008) 388–396.
[35] M. Cooper, S. Middleburgh, R. Grimes, Modelling the thermal conductivity of (U x Th 1−x) O 2 and (U x Pu 1−x) O 2, J. Nucl. Mater. 466 (2015) 29–35.
[36] P.G. Klemens, Theory of thermal conduction in thin ceramic films, Int. J. Thermophys. 22 (1) (Jan 2001) 265–275 (in English).
[37] A.J.H. McGaughey, A. Jain, Nanostructure thermal conductivity prediction by Monte Carlo sampling of phonon free paths, Appl. Phys. Lett. 100 (6) (2012) 061911.
[38] W. Bradshaw, C. Matthews, Properties of refractory materials, 1958. Collected Data and References, IMSD-2466.
[39] J. Weilbacher, Measurement of Thermal Diffusivity of Mixed Uranium Plutonium Oxides, vol. 4, High Temp High Press, 1972, pp. 431–438.
[40] P.S. Murti, C. Mathews, Thermal diffusivity and thermal conductivity studies on thorium-lanthanum mixed oxide solid solutions, J. Phys. D Appl. Phys. 24 (12) (1991) 2202.
[41] R.K. Behera, C.S. Deo, Atomistic models to investigate thorium dioxide (ThO2), J. Phys. Condens. Matter 24 (21) (2012) 215405.
[42] M. Rahman, B. Szpunar, J. Szpunar, The induced anisotropy in thermal conductivity of thorium dioxide and cerium dioxide, Mater. Res. Express 4 (7) (2017) 075512.
[43] B. Szpunar, J. Szpunar, K.-S. Sim, Theoretical investigation of structural and thermo-mechanical properties of thoria, J. Phys. Chem. Solid 90 (2016) 114–120.
[44] H.Y. Xiao, Y. Zhang, W.J. Weber, Thermodynamic properties of CexTh 1− xO 2 solid solution from first-principles calculations, Acta Mater. 61 (2) (2013) 467–476.
[45] G. Slack, H. Ehrenreich, F. Seitz, D. Turnbull, Solid State Phys. 34 (1979) 1. New York: Academic.
[46] Y. Lu, Y. Yang, P. Zhang, Thermodynamic properties and structural stability of thorium dioxide, J. Phys. Condens. Matter 24 (22) (2012) 225801.
[47] L. Malakkal, B. Szpunar, J.C. Zuniga, R.K. Siripurapu, J.A. Szpunar, First principles calculation of thermo-mechanical properties of thoria using Quantum ESPRESSO, Int. J. Comput. Mater. Sci. Surf. Eng. 5 (02) (2016) 1650008.
[48] B. Szpunar, J. Szpunar, Theoretical investigation of structural and thermo-mechanical properties of thoria up to 3300 K temperature, Solid State Sci. 36 (2014) 35–40.
[49] B. Szpunar, L. Malakkal, S. Chung, M.M. Butt, E. Jossou, J.A. Szpunar, Accident Tolerant Composite Nuclear Fuels, in MATEC Web of Conferences, vol. 130, EDP Sciences, 2017, p. 03001.
[50] E. Swartz, R. Pohl, Thermal boundary resistance, Rev. Mod. Phys. 61 (3) (1989) 605.
[51] D.G. Cahill, R. Pohl, Lattice vibrations and heat transport in crystals and glasses, Annu. Rev. Phys. Chem. 39 (1) (1988) 93–121.
[52] V. Sobolev, S. Lemehov, Modelling heat capacity, thermal expansion, and thermal conductivity of dioxide components of inert matrix fuel, J. Nucl. Mater. 352 (1) (2006) 300–308.
[53] E. Eser, H. Koc, M. Gokbulut, G. Gursoy, Estimations of heat capacities for actinide dioxide: uo 2, npo 2, tho 2, and puo 2, Nucl. Eng. Tech. 46 (6) (2014) 863–868.
[54] J. Southard, A Modified Calorimeter for High Temperatures. The Heat Content of Silica, Wollastonite and Thorium Dioxide Above 25° 1, 2, J. Am. Chem. Soc. 63 (11) (1941) 3142–3146.
[55] R. Agarwal, R. Prasad, V. Venugopal, Enthalpy increments and heat capacities of ThO 2 and (Th y U (1−y)) O 2, J. Nucl. Mater. 322 (2) (2003) 98–110.
[56] J. Fink, Enthalpy and heat capacity of the actinide oxides, Int. J. Thermophys. 3 (2) (1982) 165–200.
[57] Y. Lu, Y. Yang, F. Zheng, B.-T. Wang, P. Zhang, Electronic, mechanical, and thermodynamic properties of americium dioxide, J. Nucl. Mater. 441 (1) (2013) 411–420.
[58] R. Prasher, T. Tong, A. Majumdar, An acoustic and dimensional mismatch model for thermal boundary conductance between a vertical mesoscopic nanowire/nanotube and a bulk substrate, J. Appl. Phys. 102 (10) (2007) 104312–104410.
[59] S. Hepplestone, G. Srivastava, Low-temperature mean-free path of phonons in carbon nanotubes, J. Phys. Conf. 92 (2007) 012076. IOP Publishing.
[60] H. Kim, M.H. Kim, M. Kaviany, Lattice thermal conductivity of UO2 using ab-initio and classical molecular dynamics, J. Appl. Phys. 115 (12) (2014) 123510.
[61] J.W. Pang, W.J. Buyers, A. Chernatynskiy, M.D. Lumsden, B.C. Larson, S.R. Phillpot, Phonon lifetime investigation of anharmonicity and thermal conductivity of UO 2 by neutron scattering and theory, Phys. Rev. Lett. 110 (15) (2013) 157401.